1-31-2007

Induction electrohydrodynamics micropump forhigh heat flux cooling

Vishal Singhal

S V. Garimella
Purdue University, sureshg@purdue.edu

Induction Electrohydrodynamics Micropump for High Heat Flux Cooling[1]

Vishal Singhal and Suresh V. Garimella[2]
School of Mechanical Engineering, Purdue University
585 Purdue Mall, West Lafayette, IN 47907-2088   USA

ABSTRACT

Induction electrohydrodynamics (EHD) has been investigated as a possible means of pumping liquids through microchannel heat sinks for cooling microprocessors. A pump utilizing induction EHD has been microfabricated and tested. The experimental results matched the predictions from correlations to within 30%. Based on this, a micropump has been designed which is miniaturizable to a level where it can be integrated into the microchannels. The micropump utilizes a vibrating diaphragm along with induction EHD for pumping. The vibrating diaphragm does not cause any net flow by itself but causes high local bulk fluid velocities which lead to an increase in the power drawn from the electrodes and therefore, an increase in efficiency of EHD, both of which lead to a higher flow rate. The performance of the pump is predicted using an experimentally validated numerical model. The numerical model solves the three-dimensional transient fluid flow and charge transport problem due to simultaneous actuation of EHD and the vibrating diaphragm. Numerical results for micropumps integrated into trapezoidal microchannels are presented. The results indicate that the proposed micropump design has significant potential for microelectronics cooling applications: It is easy and inexpensive to fabricate, needs no added space, and can achieve the high flow rates needed.

[2] To whom correspondence should be addressed: sureshg@purdue.edu, (765) 494 5621

1. INTRODUCTION

Liquid cooling of microprocessors using microchannel heat sinks requires pumps for actuating the liquid flow. Since these pumps would be used in desktops, laptops and other mobile computing devices, they must be small, light-weight and low-cost. Several micro- and meso-scale pumps have been proposed in the literature for this application, and some have been implemented in practical applications [1, 2]. A review of micropumps for electronics cooling was compiled in [3].

The micropump design presented here is developed for *integrated* microchannel cooling systems, where micropumps are integrated into the microchannels as opposed to being the stand-alone units typical of most designs [4]. Induction EHD [5] is investigated as a means of pumping in microchannels. Experiments are performed to show that induction EHD in microscale channels is possible and is well predicted by conventional theory. These experiments are described in detail in Section 2. The main advantage of this system, in addition to the savings in size and weight, is the significantly lower cost which can result from the fact that its fabrication requires standard silicon micromachining techniques and can be integrated with that of the microchannels [6].

A micropump design for integrated microchannel cooling systems based on induction EHD was presented by the authors in [7, 8]. An improved design, better suited to integration, is presented here. The pump presented in [7, 8] used a circular pumping chamber and gradually expanding/contracting nozzle-diffuser elements. The purpose of this design was to create extra flow using flow rectification from nozzle-diffuser elements. The present design is based on a straight channel, so that the pumping chamber is rectangular, and no nozzle-diffuser elements are used. Instead of relying on flow rectification, the present design exploits the increase in power

output from induction EHD due to high instantaneous flow velocities created by the vibrating diaphragm. A detailed explanation of the working principle of the present micropump is given in Section 3. Numerical modeling results used to estimate the performance of the pump are also presented.

2. EXPERIMENTAL DEMONSTRATION AND NUMERICAL MODELING OF EHD MICROPUMPING

A micropump based on repulsion-type induction EHD was fabricated using the microfabrication techniques described in [9]. The fabrication procedure consists of the following three main steps (as shown in Figure 1):

1. Fabrication of arrays of parallel electrodes,

2. Deposition of the isolation layer with holes for contact spots, and

3. Fabrication of contact pads and bus-bars to contact every third electrode.

The parallel electrodes used to create the traveling electric field were fabricated by evaporating a 500 nm-thick aluminum layer, followed by photolithography using positive photoresist (Figure 1b). The isolation layer was created by spinning-on PI2771 photosensitive polyimide from HD MicroSystems. It prevents contact of the liquid with the electrodes, which can cause electrical shorting between the electrodes. Contact spots for electrodes were etched into the isolation layer using photolithography (Figure 1c). Finally, 250 nm of aluminum was sputtered on, and the bus-bars and the contact pads were patterned on this layer (Figure 1c). The bus-bars are used to contact every third electrode to the same voltage line; the contact pads are used to supply voltage to the parallel electrodes.

3

Fabrication was carried out in the Microelectronics and Nanotechnology Research Laboratory at Purdue University. A photograph of one of the dies on the finished wafer is shown in Figure 2. The width of each electrode is 12 μm, while the spacing between adjacent electrodes is 18 μm. The length of the electrodes is 8 mm.

2.1. Experimental Set-Up

A schematic of the experimental set-up is shown in Figure 3. It consists of several different components: Micromanipulator probe station, three micromanipulator test positioners, microscope connected to the micromanipulator stage, video camera, three-phase power switching circuit, high-voltage power supply, oscilloscope and heater power supply. Details of the experimental set-up including specifications of components and vendors are available in [6].

Deionized water mixed with a small mount of potassium chloride (KCl) to increase its conductivity was used in the experiments. The electrical conductivity of the liquid was measured using an electrochemistry meter and a conductivity cell. The conductivity cell has a cell constant of 0.56 cm^{-1} and can measure conductivity values from 0.01 to 3×10^5 μS/cm, accurate to ±0.5% of the reading. The conductivity of the solution used in the experiments was 16.6 μS/cm at 21.8°C. The temperature coefficient of conductivity for the water-KCl solution is 0.022°C^{-1} [10].

The fluid velocity was measured by tracking small polystyrene particles (1.5 μm mean diameter) entrained in the fluid. The particles were obtained as an aqueous suspension with 10% solids by weight. This suspension was mixed into the working fluid for the experiments such that the volume concentration of the suspension was 0.01%.

The walls around the electrodes were made from thin, clear mica sheets. Three mica sheets were used as shown in Figure 4a. Each 25.4 mm × 25.4 mm mica sheet had a thickness of 25 μm, with a variability of up to ±10% in thickness. Rectangular holes of dimensions 15.9 mm × 17.5 mm were cut in two of the mica sheets. The third mica sheet was used to cover the well created by these two mica sheets. The two mica sheets with holes were stacked on top of the device so that their side walls created a well around the device, as shown in Figure 4b. The contact pads need to be connected to the micromanipulator test positioners for powering the electrodes, and hence were not covered by the mica sheets.

2.2. Experimental Procedure

The experiment was set up as shown in Figure 3. A circular thin-film heater of diameter 12.7 mm was attached with Kapton tape to the back side of the die under test. The heater has a total electrical resistance of 3.8 Ω and is rated to 3.3 V, 0.9 A and 3 W. A 3-phase voltage from the power switching circuit was applied to the contact pads of the test die through micromanipulator test positioners. The two hollowed mica sheets were placed over the die being tested to create a well as shown in Figure 4b. The test liquid (deionized water mixed with KCl and polystyrene particles) was introduced into the well using a disposable syringe and the well was then covered with the third mica sheet (with no hole). The high-voltage power supply and the 3-phase power switching circuit were then turned on. The frequency of the 3-phase power switching circuit was set to the desired value (373 kHz for the present case). This frequency corresponds to the maximum flow rate for the fluid with electrical conductivity of 16.6 μS/cm calculated as $f = \sigma_{avg}/(2\pi\varepsilon)$ [5], where σ_{avg} is the average electrical conductivity of the fluid and ε is the permittivity of the fluid. The power supply to the thin-film heater was then turned on, resulting

in an almost instantaneous motion of the polystyrene particles which is recorded using the video camera.

The recorded video in analog format is converted to digital format and the resultant digital video file is converted into individual images, with each image representing one frame. The images were used to perform a particle image velocimetry (PIV) analysis [11] using the research software EDPIV [12]. A traditional correlation-based interrogation approach was used [13]. Fast Fourier transforms were used to accelerate the method. The velocity fields as well as the mean and the maximum velocities in the two in-plane directions were obtained by this means.

2.3. Experimental Results

Experiments were performed on different dies using fluid of the same electrical conductivity. Values for all the relevant experimental parameters are provided in Table 1. The variation with molar concentration of the electrical conductivity of the aqueous solution of KCl is presented for three different temperatures in Figure 5 [14].

During the experiments, it was observed that the velocity of the polystyrene particles started decreasing after approximately 5 seconds, almost to zero, and fluid circulation in the well ceased. Instead, the fluid was pumped toward the end of the electrodes causing a pressure head against which the fluid must now work. This causes the observed decrease in the fluid velocity. Indeed, if the traveling potential wave was turned off at this point, this generated pressure head caused flow in the opposite direction. Since the aim of this work was to generate and measure fluid velocity in the absence of external pressure gradients, the PIV analysis was confined to the flow during the initial five-second period.

6

The velocity field measured in a typical experiment is presented in Figure 6. It is noted that almost all the velocity vectors except for those in the top row point directly downward. This implies that the fluid motion was perpendicular to the electrodes as expected. The time-averaged maximum downward fluid velocity (perpendicular to the electrodes) was 19.4 μm/sec and was observed to occur at the location (85.33 μm, 53.33 μm); the time-averaged velocity, averaged over the observation window area shown in Figure 6, was 12.3 μm/sec.

The PIV images were obtained with a microscope of 25X magnification and 0.31 numerical aperture. These parameters, along with the average wavelength of visible light (550 μm), average size of the tracking particles (1.5 μm) and refractive index of water (1.33), were used to calculate the experimental uncertainty in the position of the particles and the depth of field [15]. The uncertainty in position was 317.60 nm and that in the depth of field was 7.61 μm. Since 150 images were used for the PIV analysis, the uncertainty in velocity was 0.78 μm/sec.

2.4. Model Predictions

The micropump set-up considered in the experiments was modeled and the theoretical maximum fluid velocity estimated [5]. The modeling was accomplished in two steps. First, a numerical model was used to solve the transient heat transfer problem to obtain the temperature difference across the liquid layer. In the second step, the electrical conductivity gradient corresponding to the temperature gradient obtained in the first step was used to estimate the maximum fluid velocity for the geometry considered.

The transient, three-dimensional heat transfer model was implemented in the commercial software package FIDAP [16]. The physical domain considered is shown in Figure 7a. All the heat generated in the thin-film heater is either lost to its underside by convection, or conducted

through the quartz wafer, water and mica sheet and convected to air from the top side of mica sheet. Since the whole set-up is at ambient temperature at the start of the experiments, some heat is also absorbed by the quartz, water and mica due to their thermal capacitances. Some heating is caused due to the electrodes as well; however, this effect would be small and is neglected in simulations. This is evident from the fact that powering the electrodes in the absence of thin-film heating does not cause any pumping action.

Convection heat transfer at the bottom and top of the domain is modeled using the following equations, respectively [17]:

$$\overline{Nu_L} = 0.27 Ra_L^{1/4} \qquad (1)$$

$$\overline{Nu_L} = 0.54 Ra_L^{1/4} \qquad (2)$$

These equations are valid for $10^4 \leq Ra_L \leq 10^7$, which is satisfied in the present case. The average Nusselt number is given by $\overline{Nu_L} = \overline{h}L/k_{air}$, Rayleigh number by $Ra_L = g\beta_{air}(T_s - T_\infty)L^3/\nu_{air}\alpha_{air}$ and characteristic length by $L = A_s/P$; $\overline{h}$ is the mean convection heat transfer coefficient, A_s the surface area, P the perimeter of the region of interest (quartz wafer for convection through the bottom mica sheet for convection through the top of the domain), T_∞ the ambient temperature, and T_s the temperature of the quartz wafer or the mica sheet. The thermal properties of quartz, water, air [17] and mica [18] used in model are summarized in Table 2.

The forced convection heat transfer between water in the well and the quartz wafer below and mica sheet was neglected; this assumption is justified later. The boundary conditions used in the analysis were as follows. One-dimensional conduction was assumed through the thickness of the solid walls and water. Hence the vertical boundaries of the domain, as well as the vertical interfaces between the mica walls and water, were modeled as being adiabatic. Furthermore, the

heat transfer coefficient on the top and bottom of the domain were uniform. The uniform heat flux at the top of the mica sheet was calculated using: $q''_{top} = \overline{h_{top}}\left(T_{s,top} - T_\infty\right)$, while the flux at the bottom of the quartz wafer was calculated using $q''_{bottom} = \left(q_{heater}/A_s\right) - \overline{h_{bottom}}\left(T_{s,bottom} - T_\infty\right)$. Since $T_{s,top}$ and $T_{s,bottom}$ are not known a priori, application of these two boundary conditions is an iterative process.

A mesh and time-step independence analysis was performed based on the predicted temperatures at the ends of the well of water, i.e., at the surfaces of the quartz wafer and mica sheets which are in contact with water. A mesh size of 2×2×115, with 115 elements along the depth of the well, and a time step of 0.1 second were used. Since one-dimensional conduction through the water is assumed, there is no variation in temperature in the two orthogonal directions and hence only a 2×2 mesh is sufficient. Less than 1% variation in temperatures at the ends of the water well was observed when the mesh size was doubled in each direction and the time-step halved. The computed temperature difference across the water well is plotted as a function of time in Figure 7b. The time scale starts when the thin-film heater is powered on. The temperature difference reaches 0.018 °C in less than half a second after heating starts, and remains between 0.018 °C and 0.019 °C for the next five seconds over the time period of interest.

The assumption neglecting forced convection between water in the well and the containing walls is now verified. The relative significance of free and forced convection is estimated by calculating Gr_L/Re_L^2, where Gr_L is the area-averaged Grashof number and is given by $Gr_L = g\beta_{water}\left(T_s - T_{water}\right)L^3/\nu_{water}^2$. Thermophysical properties of water used for calculating Gr_L and Re_L are given in Tables 1 and 2. The mean temperature difference between water and the

9

adjoining surface is assumed to be 0.01°C (≈ 0.019/2) for calculating Gr_L and the maximum fluid velocity of 19.4 μm/sec is used for calculating Re_L. This results in $Gr_L = 2.66$ and $Re_L = 9.71 \times 10^{-2}$, so that $Gr_L/Re_L^2 = 281.8$. Since $Gr_L/Re_L^2 \gg 1$, forced convection is negligible relative to free convection.

The temperature difference of 0.018°C calculated above was used to calculate the maximum velocity in the well, using the analytical model of Melcher and Firebaugh [5]. The analytical model in [5] is for fully developed flow between parallel plates maintained at different constant temperatures. The plate at the lower temperature is maintained at zero potential while a traveling sinusoidal potential wave is applied to the one at the higher temperature. The expression for the time-averaged velocity profile is reproduced below from [5]:

$$v_x = Dd \left[F \int_0^\zeta \frac{d\zeta}{\mu(\zeta)} - \int_0^\zeta \frac{f(\zeta)}{\mu(\zeta)} d\zeta \right] \tag{3}$$

where, $\quad D = \varepsilon k \hat{V} \hat{V}^* / \left[4d \left(\cosh b_r - \cos b_i \right) \right], \quad F = \int_0^1 f(\zeta)/\mu(\zeta) d\zeta \bigg/ \int_0^1 d\zeta/\mu(\zeta), \quad$ and

$f(\zeta) = e^{-a_r(\zeta-1)} \left[b_r \sin(b_i\zeta) - b_i \sinh(b_r\zeta) + a_i \left(\cosh(b_r\zeta) - \cos(b_i\zeta) \right) \right]$. Here, $\zeta = y/d$ is the nondimensional distance from the plate at the lower temperature, d is the absolute distance between the plates, $a_r = \eta/(1+S^2)$, $a_i = -\eta S/(1+S^2)$, $b_r = A\cos(\theta/2)$ and $b_i = -A\sin(\theta/2)$.

In the expressions for b_r and b_i, $A = \left\{ \left[4(kd)^2 + \eta^2 \left(1-S^2 \right) / \left(1+S^2 \right)^2 \right]^2 + \left[2\eta^2 S / \left(1+S^2 \right)^2 \right]^2 \right\}^{1/4}$,

and $\theta = \tan^{-1} \left\{ \left[2\eta^2 S / \left(1+S^2 \right)^2 \right] \bigg/ \left[4(kd)^2 + \eta^2 \left(1-S^2 \right) / \left(1+S^2 \right)^2 \right] \right\}$. Here, $\eta = \Delta\sigma/\sigma_{avg}$ is the ratio of the electrical conductivity difference between the top and bottom plates to the average electrical conductivity of the fluid between the plates, $S = \omega\varepsilon/\sigma_{avg}$, and $k = 2\pi/\lambda$. The

10

parameter values used in computations with the above expression are the same as the experimental parameters given in Table 1. The electrical conductivity difference across the water well can be calculated using $\Delta\sigma = \alpha\Delta T\sigma_{avg} = 7.30\times10^{-7} \; S/m$, in which α is the thermal coefficient of diffusivity and for water with KCl, it is 0.022 °C [10].

Equation (3) was solved numerically using the parameter values given in Table 1. A maximum fluid velocity of 26.37 µm/sec was obtained. This compares reasonably well with the maximum fluid velocity of 19.4 µm/sec obtained in the experiments. The difference between predicted and experimental velocities of about 30% can be attributed to the following reasons, all of which would cause the predicted flow velocity to be higher:

1. Equation (3) is strictly valid only for flow between parallel plates without any external pressure gradient. There is a small pressure head inherent in the experimental set-up.

2. The expression for the time-averaged velocity profile (Equation (3)) was derived for a continuous sinusoidal potential wave. The potential wave in the experiments was rectangular with a triangular leading edge, and discontinuous.

3. The electrodes were covered with a thin polyimide layer (approximately 5 µm in thickness), which would cause a slight decrease in the electric field in the fluid.

4. The depth of field of the optical system used for experimentation is 7.61 µm. Hence the experimentally observed velocities are averaged over a 7.61 µm deep slice of the fluid, such that contributions from lower velocities near the walls yield a lower value of maximum velocity from the PIV analysis than is actually realized in the experiment.

The close match between the maximum fluid velocity obtained in the experiments with that predicted from theory shows that induction EHD at the microscale is well-predicted by conventional thoery.

3. NEW MICROPUMP DESIGN

The new micropump design, as shown in Figure 8a, is based on induction EHD, where charges are induced due to the presence of a traveling electric field in a fluid subjected to an electrical conductivity gradient orthogonal to the traveling electric field [5]. The micropumps are integrated into trapezoidal microchannels, which have been chosen for their ease of fabrication using anisotropic wet-etching. Other microchannel cross-sections, including rectangular, could be equivalently used. Since the fluid in the microchannels is heated from below, a temperature gradient exists in the fluid which causes an electrical conductivity gradient. The traveling electric field is created by an array of parallel electrodes, which in the present design are deposited on the bottom side of the lid covering the microchannels, as shown in Figure 8b. The traveling electric field causes induction of ions in the bulk of the fluid. Coulomb forces cause the induced ions to move in the same direction as the traveling potential wave if the fluid close to the electrodes is at a lower electrical conductivity, corresponding to the lower temperature; this is called attraction-type induction EHD. (Repulsion-type induction EHD refers to the alternative case where the fluid flows in the direction opposite to the traveling potential wave, as used in the experiment described above.) Momentum transfer due to repeated collisions of the ions with neutral molecules leads to motion of the bulk fluid, which gives rise to the pumping action. The present pump design (Figure 8) uses attraction-type induction EHD, since the electrodes are located in proximity to the fluid with the lower electrical conductivity.

The vibration of small patches of piezoelectric material deposited on top of the lid covering the microchannels causes bulk motion of the fluid in both directions along the microchannels, and by itself causes no net flow. However, simultaneous actuation of the vibrating diaphragm

and induction EHD leads to a higher net flow rate than that due to induction EHD alone. This increase is due to the higher instantaneous bulk fluid velocity caused by the vibrating diaphragm, which leads to higher power output from induction EHD, as demonstrated in [19]. The higher power output was shown to be attributable to the combined effect of increased power drawn from the electrodes and higher efficiency of EHD [19].

3.1. Numerical Modeling

The performance of this new micropump design was analyzed using a transient, three-dimensional finite element model which was reported earlier in [7, 8]. The model solves the coupled unsteady charge transport, continuity, and Navier-Stokes equations presented in order below. It may be noted that the Navier-Stokes equations are modified to include an extra term because of Coulomb forces.

$$\partial q/\partial t + \vec{\nabla}\cdot\left(q\vec{v}\right) = \vec{\nabla}\cdot\left(\sigma\vec{\nabla}\Phi + q\mu\vec{\nabla}\Phi + D_{IA}\vec{\nabla}q\right) \tag{4}$$

$$\frac{\partial\rho}{\partial t} + \vec{\nabla}\cdot\rho\vec{v} = 0 \tag{5}$$

$$\frac{\partial\rho\vec{v}}{\partial t} + \left(\vec{v}\cdot\vec{\nabla}\right)\vec{v} = -\vec{\nabla}p + \vec{\nabla}\cdot s_{ij} + \rho\vec{F} - q\vec{\nabla}\Phi \tag{6}$$

In these equations, Φ is the potential, q the free charge density in the fluid, v the fluid velocity, D_{IA} the charge diffusion coefficient, ρ the density of the fluid, μ the fluid viscosity, p the static pressure, s the stress and F the force.

The vibrating diaphragm was modeled by specifying its position and velocity as a function of time, through user-defined subroutines. The mode shape for the first mode of vibration was used to describe its position and its temporal derivative was used as the velocity of the diaphragm [6]. A spines approach was used for remeshing. The effect of fluid-structure interaction on

13

diaphragm motion was neglected. The modeling parameters for the micropump are listed in Table 3.

3.2. Modeling Results

Simulations were performed for pump widths of 100 and 200 μm. Since the pump spans the width of the microchannel, the pump width is the same as the microchannel width. A mesh-independence analysis was performed by simulating flow due to the action of EHD alone for three different grid sizes (designated coarse, fine and finest) for a pump of width 200 μm: the coarse grid had 75 elements along the length of the pump, 20 across the width and 10 across the height for a total of 15,000 elements, while the fine grid had twice the number of nodes in every direction as compared to the coarse grid for a total of 120,000 elements. The finest grid has twice again the number of nodes in every direction as compared to the fine grid for a total of 960,000 elements.

The results are plotted in Figure 9a as a function of time for all three grid sizes. The flow rate from the fine grid was 55% lower than that from the coarse grid at the largest time considered, $t = 31.5$ μs, while flow rates predicted from the fine grid and the finest grid are within 0.5% of each other. Hence results from the fine mesh are considered mesh-independent. Further, flow rates as a function of time for the coarse grid and the fine grid are plotted in Figure 9b over a period over which the flow reached almost steady-state, $t = 1.87$ ms. The steady-state flow rates obtained from the two grids are within 9%. Hence the steady-state flow rate from the coarse mesh is expected to be within 9-10% of the mesh-independent results. Similar mesh-independence behavior is expected for the combined action of the vibrating diaphragm and induction EHD, as was observed in [8], and for the pump of width 100 μm.

The assumption regarding negligible flow-structure interaction in the model is validated next. The effect of flow-structure interaction, i.e., change in diaphragm vibration due to motion of the fluid is estimated and compared to the total vibration of the diaphragm. For flow solely due to the vibrating diaphragm in the pump of width 100 μm, the amplitude of variation of the average pressure exerted by the fluid on the diaphragm was obtained from the numerical model to be 6591.8 Pa. The deflection of the diaphragm due to this force was calculated using the software package ANSYS [20] to be 5.44×10^{-13} m. Since this deflection is much smaller than the amplitude of diaphragm vibration (1×10^{-7} m), the assumption regarding negligible flow-structure vibration is considered valid.

The net flow rates due to the action of induction EHD alone and from the combined action of the vibrating diaphragm and induction EHD, from the 100 μm-wide pump are shown in Figure 10a, over a period during which the flow reached almost steady-state. The flow due to the action of the vibrating diaphragm alone causes flow with a sinusoidal variation, even though the net flow is zero. The amplitude of this variation is 2.5×10^{-10} m^3/sec corresponding to a maximum Reynolds number of 5.67. The flow rate due to combined action of the vibrating diaphragm and induction EHD is 13% higher (3.33×10^{-11} m^3/sec) than that due to induction EHD alone (2.91×10^{-11} m^3/sec, Figure 10a). It may be noted that this increase is solely due to the increase in the output of the EHD action, partially due to increased efficiency and partially due to increased power drawn from the electrodes. A similar figure comparing the net flow rates due to the action of induction EHD alone to that from the combined action of the vibrating diaphragm and induction EHD for a 200 μm-wide pump is shown in Figure 10b. Here the steady-state net flow rate due to combined action of the vibrating diaphragm and induction EHD (1.75×10^{-10} m^3/sec) is 12% higher than the steady-state flow rate due to induction EHD alone (1.55×10^{-10} m^3/sec).

If these micropumps are integrated into all the microchannels in a heat sink, a flow rate of 1.75×10^{-10} m^3/sec from an individual micropump corresponds to a total flow rate of 0.42 ml/min for a chip of size 1 cm × 1 cm, in which the trapezoidal microchannel walls are 50 μm wide at the top of the microchannels, corresponding to a total of 40 microchannels. For reference, a heat transfer rate of 100 W/cm^2 for single-phase convective cooling with water as the working fluid under a total temperature difference between mean outlet and mean inlet fluid temperatures of 50°C requires a flow rate of 29.2 ml/min. The proposed integrated micropumps can generate a flow rate of 0.42 ml/min under these conditions and achieve a heat transfer rate of 1.44 W/cm^2. Though the cooling rate is modest, it is achieved without using an external pump. The flow rate scales linearly with the electrode width and spacing and thus can be increased by a factor of 4 by decreasing these dimensions to 5 μm each [5]. The flow rate achievable with the pump can also be significantly increased by use of fluids containing suspensions of nano-scale particles. Charges would be induced at the solid-liquid interfaces on the particles due to electrical conductivity and permittivity jumps.

3.3. Micropump Power Requirements

The power required for operation of the micropump is an important parameter and is estimated here. The efficiency of induction EHD in the present case, *i.e.*, for potential wave and electrode parameters and the fluid properties listed in Table 3, is estimated using the model described in detail in [19]. The efficiency of the pump, which is the ratio of fluidic power output to electrical power input, is approximately 0.015. The efficiency and power requirement calculations developed here neglect any entry and exit losses. The fluid power output can be calculated as a product of the pressure drop through the channels and the volume flow rate. The

pressure drop can be calculated as $\Delta p = 2\mu \dfrac{QL_d}{AD_h{}^2} C_f \mathrm{Re}$, where $C_f \mathrm{Re} = 16.4$ for trapezoidal channels with an angle of 54.7 degrees which are 200 μm wide at the top and 50 μm deep [21]. The total electrical power input is given by $P_{in} = Q\Delta p / \eta$, where η is the efficiency of EHD. The power input for all the pumps in a 1 cm × 1 cm chip calculated using this procedure is 0.32 mW. Hence the present pump design can remove 1.44 W/cm^2 with a power input of 0.32 mW, making it very attractive from the point of view of power consumption.

4. CONCLUSIONS

Integration of micropumps into microchannels has significant potential. Such integration greatly reduces the volume and weight of the microchannel cooling system. The cost of the system is also significantly lowered because fabrication of the micropump can be integrated with that of the microchannels. The novel micropump design presented here is a good candidate for such miniaturization and integration.

The numerical model predicts that the micropump design can achieve a flow rate of 10.5 μl/min of water for a pump of size 1500 μm × 200 μm × 50 μm. This corresponds to a total flow rate of 0.42 ml/min if the micropumps are integrated into forty parallel microchannels in a chip of size 1 cm × 1cm. For a total fluid temperature rise in the microchannels of 50°C, this arrangement can remove 1.44 W/cm^2 of heat at a pumping power input of 0.32 mW. The flow rate from the micropump can be significantly increased by decreasing the width and spacing of the electrodes and using fluids containing suspensions of nano-scale particles.

Further, experiments in this study show that flow due to induction EHD in microscale channels is possible and is well predicted by conventional theory. A micropump utilizing

induction EHD was designed and fabricated using silicon micromachining techniques. This micropump was tested and the experimental results matched predictions to within 30%.

Acknowledgements

References

[1] Jiang, L., Mikkelsen, J., Koo, J. M., Huber, D., Yao, S., Zhang, L., Zhou, P., Maveety, J.G., Prasher, R., Santiago, J. G., Kenny, T. W., and Goodson, K. E., 2002, "Closed-loop electroosmotic microchannel cooling system for VLSI circuits," *IEEE Transactions on Components, Packaging and Manufacturing Technology*, **25**, No. 3, pp. 347-355.

[2] Miner, A., and Ghoshal, U., 2004, "Cooling of high-power-density microdevices using liquid metal coolants," *Applied Physics Letters*, **85**, No. 3, pp. 506-508.

[3] Singhal, V., Garimella, S. V., and Raman, A., 2004, "Microscale pumping technologies for microchannel cooling systems," *Applied Mechanics Reviews*, **57**, pp. 191-221.

[4] Garimella, S. V., Singhal, V., and Liu, D., "On-chip thermal management with microchannel heat sinks and integrated micropumps," *Proceedings of the IEEE* (in press).

[5] Melcher, J.R., and Firebaugh, M.S., 1967, "Traveling-wave bulk electroconvection induced across a temperature gradient," *Physics of Fluids*, **10**, pp. 1178-1185.

[6] Singhal, V., 2005, *A Novel Micropump for Integrated Microchannel Cooling Systems*, Ph.D. Thesis, Purdue University, West Lafayette, IN.

[7] Singhal, V., and Garimella, S. V., 2004, "A novel micropump for electronics cooling," *International Mechanical Engineering Congress and Exposition*, IMECE2004-61147, Anaheim, CA, pp. 1-12.

[8] Singhal, V., and Garimella, S. V., 2005, "A novel valveless micropump with electrohydrodynamic enhancement for high heat flux cooling," *IEEE Transactions on Advanced Packaging,* **28**, No. 2, pp. 216-230.

[9] Schlitz, D.J., 2004, *Microscale Ion Driven Air Flow*, Ph.D. thesis, Purdue University, West Lafayette, IN.

[10] Fuhr, G., Hagedorn, R., Muller, T., Benecke, W., and Wagner, B., 1992, "Microfabricated electrohydrodynamic (EHD) pumps for liquids of higher conductivity," *Journal of Microelectromechanical Systems*, **1**, pp. 141-146

[11] Raffel, M., Willert, C., and Kompenhans, J., 1998, *Particle Image Velocimetry: A Practical Guide*, Springer-Verlag, Berlin, Germany.

[12] Wereley, S.T., Gui, L., and Meinhart, C.D., 2002, "Advanced algorithms for microscale velocimetry," *AIAA Journal*, **40**, pp. 1047-1055.

[13] Adrian, R.J., 1991, "Particle-imaging techniques for experimental fluid mechanics," *Annual Review of Fluid Mechanics*, **23**, pp. 261-304.

[14] Lide, D.R., Ed., 2004, *Handbook of Chemistry and Physics*, CRC Press, Boca Raton, FL.

[15] Liu, D., Garimella, S.V., and Wereley, S.T., 2005, "Infrared micro-particle image velocimetry measurement in silicon-based microdevices," *Experiments in Fluids*, **38**, pp. 385-392.

[16] FIDAP 8.7.2, 2003, *FIDAP User's Manual*, Fluent Inc, Lebanon, NH.

[17] Incropera, F.P., and Dewitt, D.P., 1998, *Fundamentals of Heat and Mass Transfer*, John Wiley & Sons, New York.

[18] Web-site of B&M Mica Co., Inc., http://www.bmclearmica.com/pg5-2.htm

[19] Singhal, V., and Garimella, S. V., 2005, "Influence of bulk fluid velocity on the efficiency of electrohydrodynamic pumping," *Journal of Fluids Engineering,* **127**, pp. 484-494.

[20] ANSYS 7.1, 2003, *ANSYS*, Ansys, Inc., Canonsburg, PA.

[21] Shah, R.K., 1975, "Laminar flow friction and forced convection heat transfer in ducts of arbitrary geometry," *International Journal of Heat and Mass Transfer*, **18**, pp. 489-462.

LIST OF TABLES

Table 1: Values of experimental parameters.

Parameter	Value
Working Fluid – Deionized water with KCl	
Permittivity, ε	7.08×10^{-10} F/m
Mean Electrical Conductivity, σ	1.66×10^{-3} S/m
Temperature Coefficient of Conductivity, α	0.022 $°C^{-1}$
Dynamic Viscosity, μ	8.55×10^{-4} N.s/m^2
Potential Wave	
Frequency	373 kHz
Phases	3
Amplitude	10 V
Wavelength	90 µm
Electrode and Electrode Section Dimensions	
Electrode Width	12 µm
Spacing between Electrodes	18 µm
Electrode Section Width	4.8 mm
Electrode Section Length	8 mm
Well Dimension	
Width	17.5 mm
Length	15.9 mm
Height	50 µm
Heater	
Heater Diameter	12.7 mm
Heater Power	0.63 W (1.5 V × 0.42 A)
Polystyrene Particles	
Polystyrene Particle Diameter	1.5 µm
Particle Weight in Suspension	10% (w/w)
Volume Concentration of Suspension	0.01 % (v/v)

Table 2: Thermal properties of various materials used to model the experimental set-up.

Parameter	Value
Quartz	
Density, ρ	2650 kg/m^3
Thermal Conductivity, k	8.3 W/m.K
Specific Heat, c_p	745 J/kg.K
Water	
Density, ρ	997 kg/m^3
Thermal Conductivity, k	0.613 W/m.K
Specific Heat, c_p	4179 J/kg.K
Mica	
Density, ρ	2900 kg/m^3
Thermal Conductivity, k	0.669 W/m.K
Specific Heat, c_p	275 J/kg.K
Air	
Kinematic Viscosity, v	15.89×10^{-6} m^2/sec
Thermal Diffusivity, α	22.5×10^{-6} m^2/sec
Thermal Conductivity, k	26.3×10^{-3} W/m.K
Ambient Temperature, T_∞	293 K
Coefficient of Thermal Expansion, β_{air}	3.41×10^{-3} K^{-1}

Table 3: Parameters used for numerical modeling.

Parameter	Value
Working Fluid – Deionized water with KCl	
Density, ρ	987.17 kg/m^3
Permittivity, ε	7.08$\times10^{-10}$ F/m
Electrical Conductivity, σ	0.20$\times10^{-3}$ S/m @ T = 0 °C
	0.70$\times10^{-3}$ S/m @ T = 72.80 °C
Dynamic Viscosity, μ	8.55$\times10^{-4}$ N.s/m^2
Potential Wave	
Frequency	122 kHz
Amplitude	200 V
Vibrating Diaphragm	
Frequency	10 kHz
Amplitude	0.1 µm
Electrode Dimensions	
Electrode Width	20 µm
Spacing between Electrodes	20 µm
Pump Dimensions	
Pump Width (at top)	100 µm / 200 µm
Pump Depth	50 µm
Pump Length	1500 µm
Vibrating Diaphragm Length	500 µm
Electrode Section Length	500 µm (Each)

LIST OF FIGURES

Cross-section   Top-view

(a)

Quartz

Al Electrodes

Electrodes

10 μm

(b)

Contact Spots

Contact Spots   Photo-sensitive Polyimide

(c)

Bus Bars

V_1 V_2 V_3

Bus Bars

(d)

Figure 1: Cross-section and top-view of: (a) quartz wafer, (b) wafer with array of parallel electrodes, (c) wafer with isolation layer having holes for contact spots, and (d) wafer with contact pads and electrodes connected to a 3-phase bus bar.

26
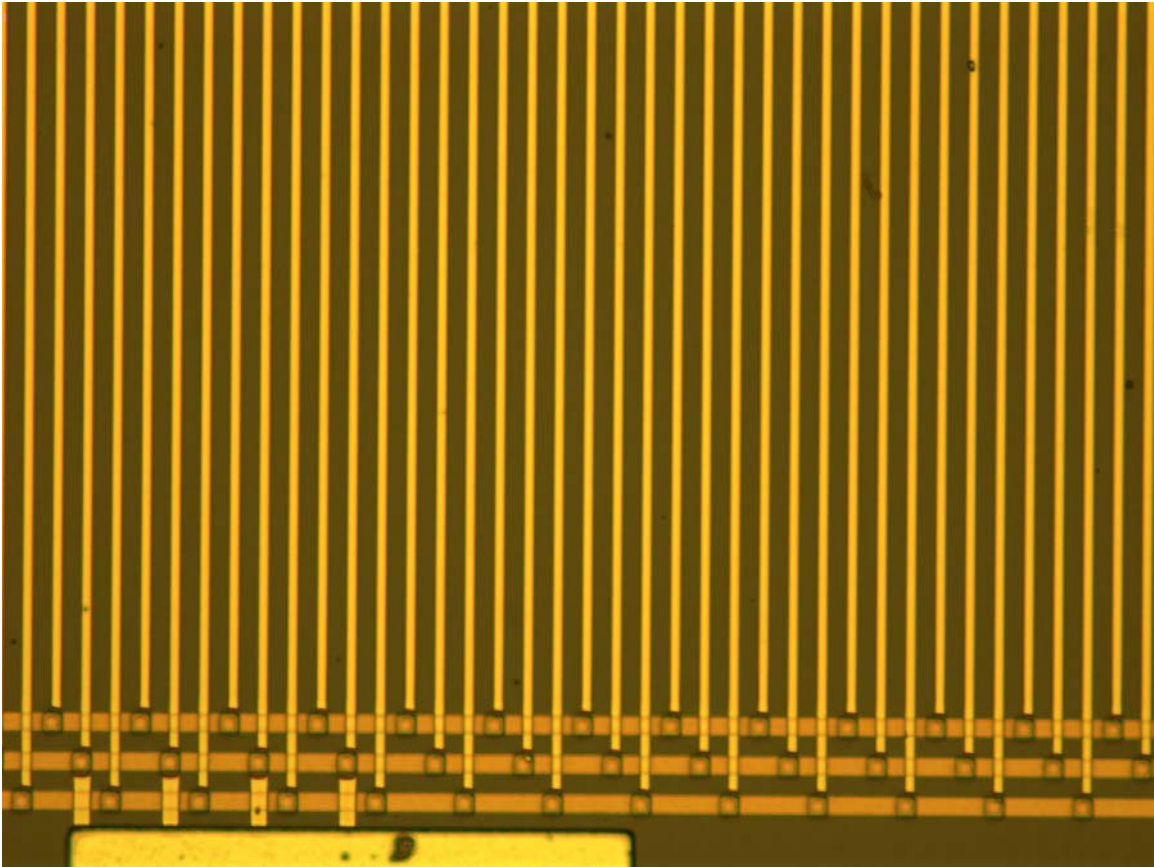
Figure 2: Photograph of one of the dies used in the experiments.
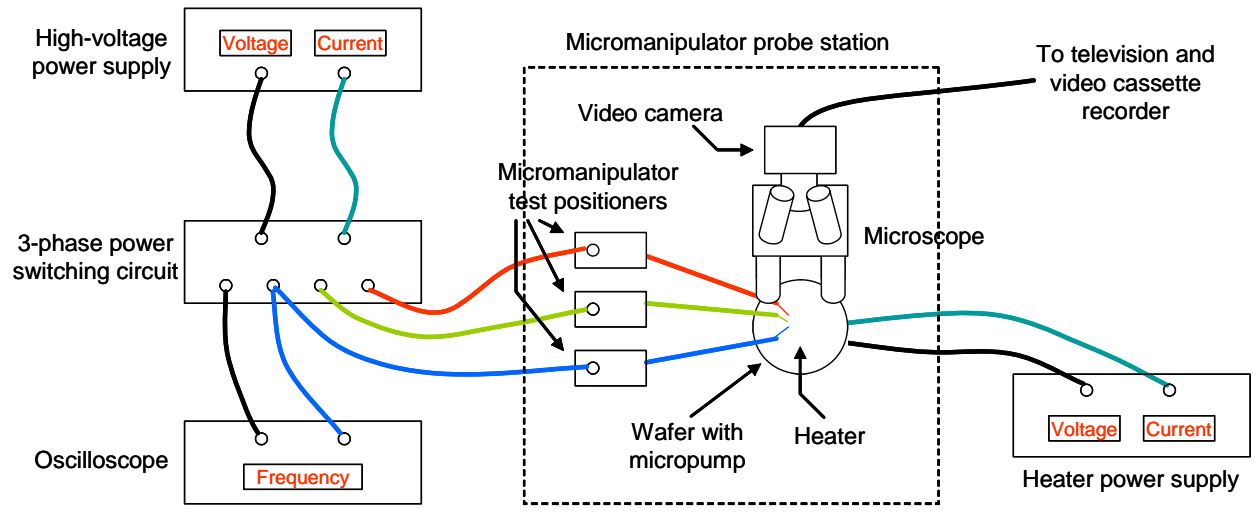
Figure 3: Schematic diagram of the experimental set-up.
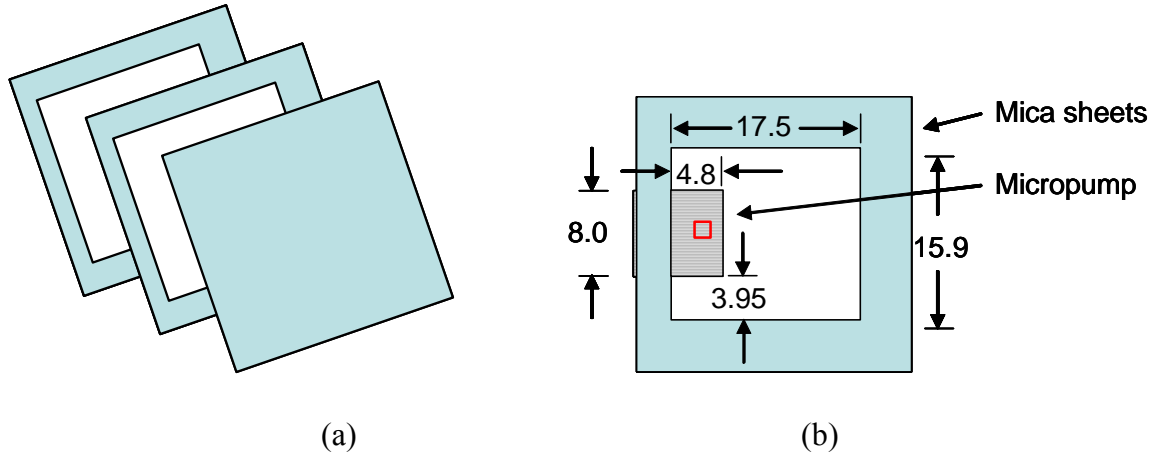
Figure 4: Mica sheets used for creating a fluid well around the electrodes: (a) Cross-section and (b) top-view of final device with mica sheets drilled for fluidic connections (all dimensions are in mm). The observation window is outlined in the electrode region.
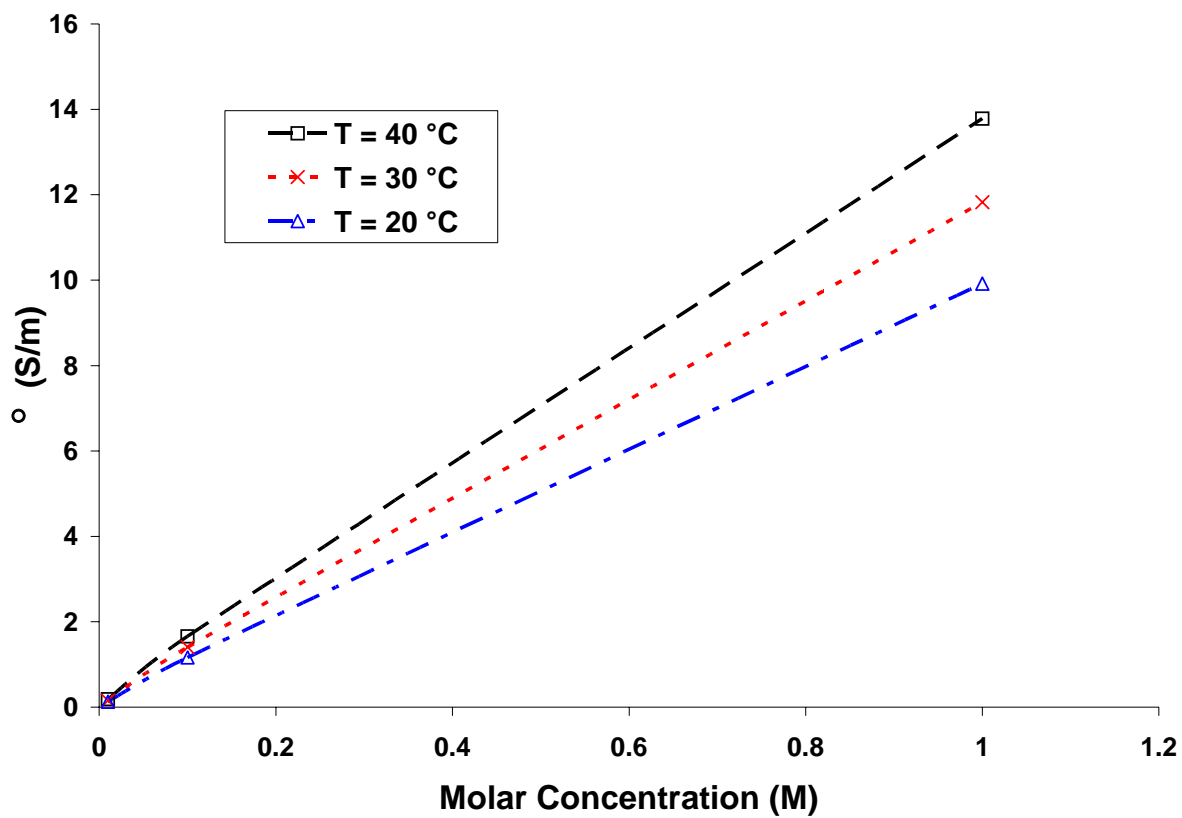
Figure 5: Variation of electrical conductivity of KCl solution with molar concentration for three different temperatures [14].
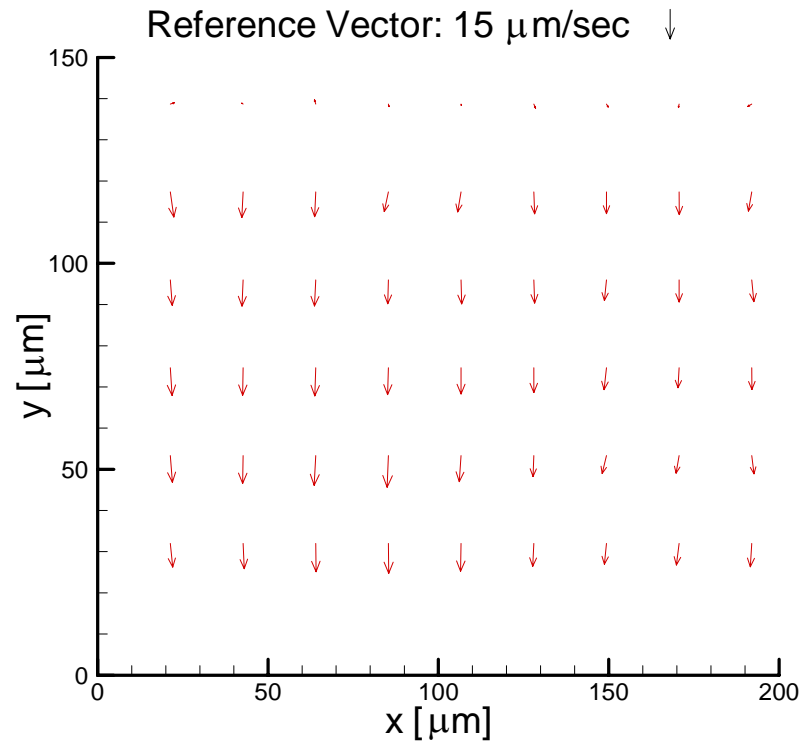
Figure 6: Velocity field obtained using PIV analysis from a typical set of experiments.
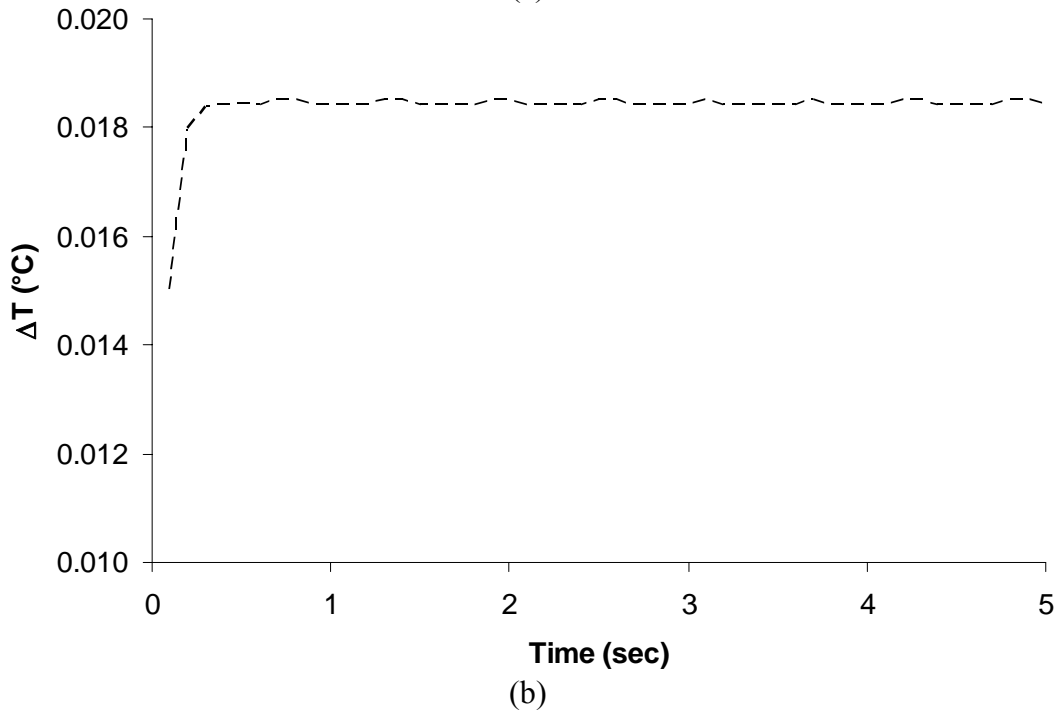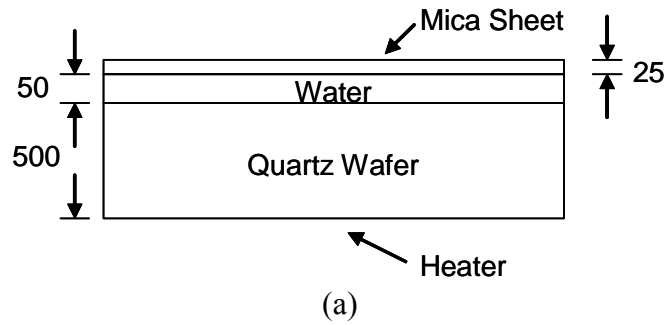
Figure 7: (a) Two-dimensional cross-section of the three-dimensional geometry modeled to simulate the experimental set-up (all dimensions are in µm), and (b) plot of temperature difference across the height of the water well as a function of time from the numerical model (time starts from zero when heating starts).
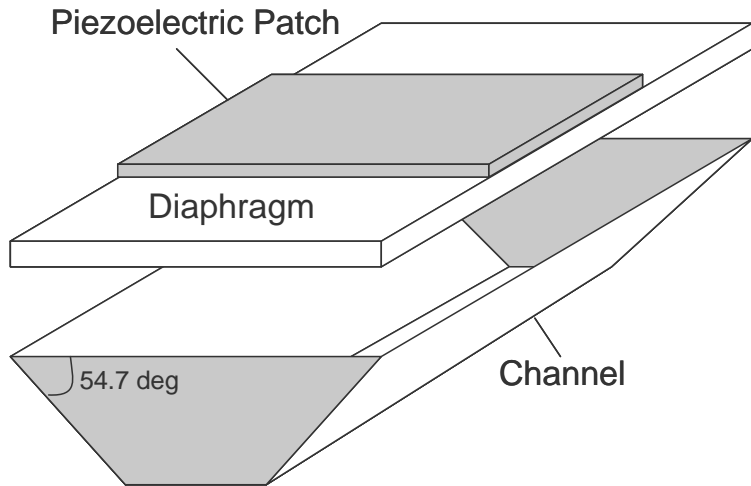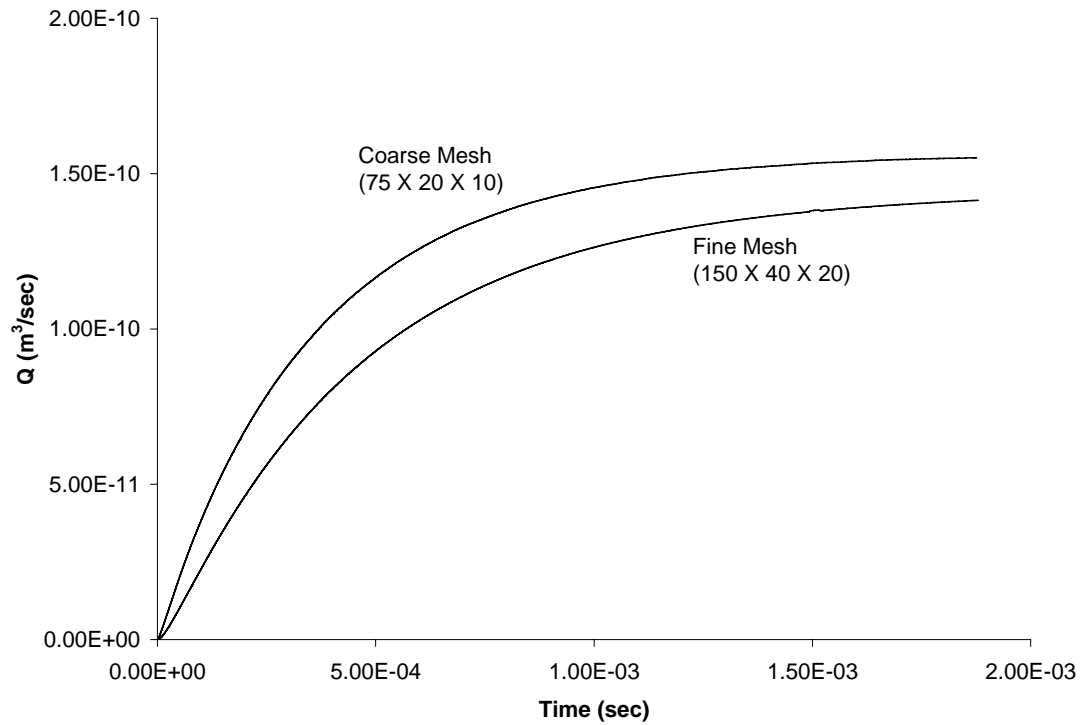
(a)

(b)
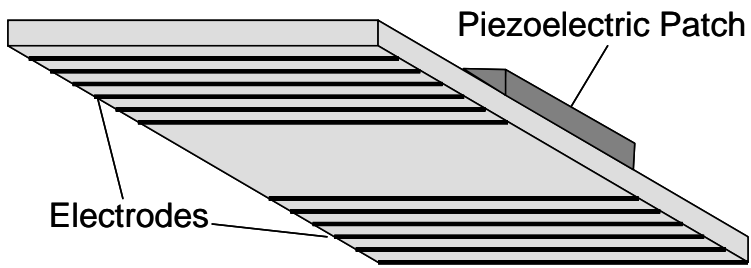
(c)

Figure 8: (a) Schematic of the new micropump design, (b) an array of microchannels, and (c) electrodes deposited on the bottom side of the lid covering the microchannels.
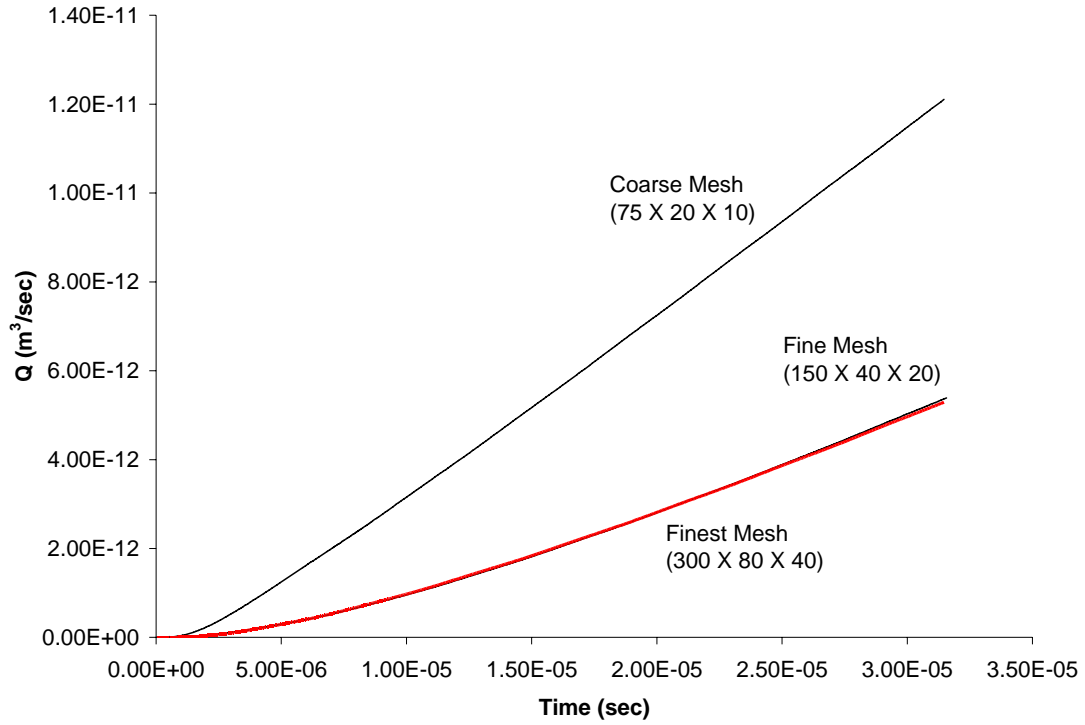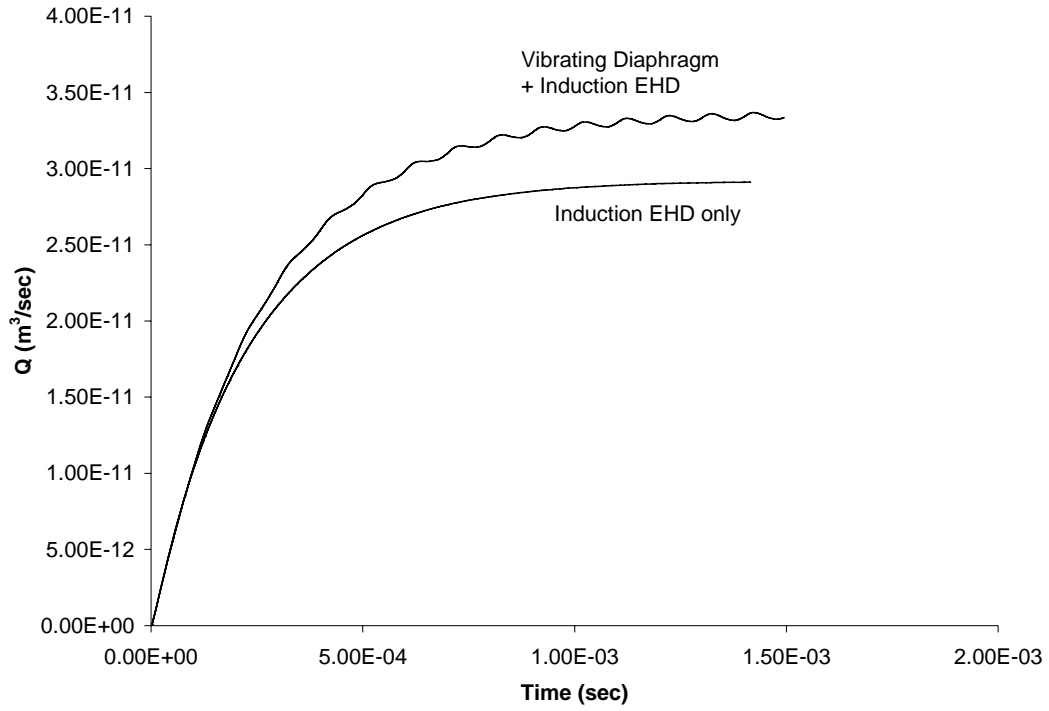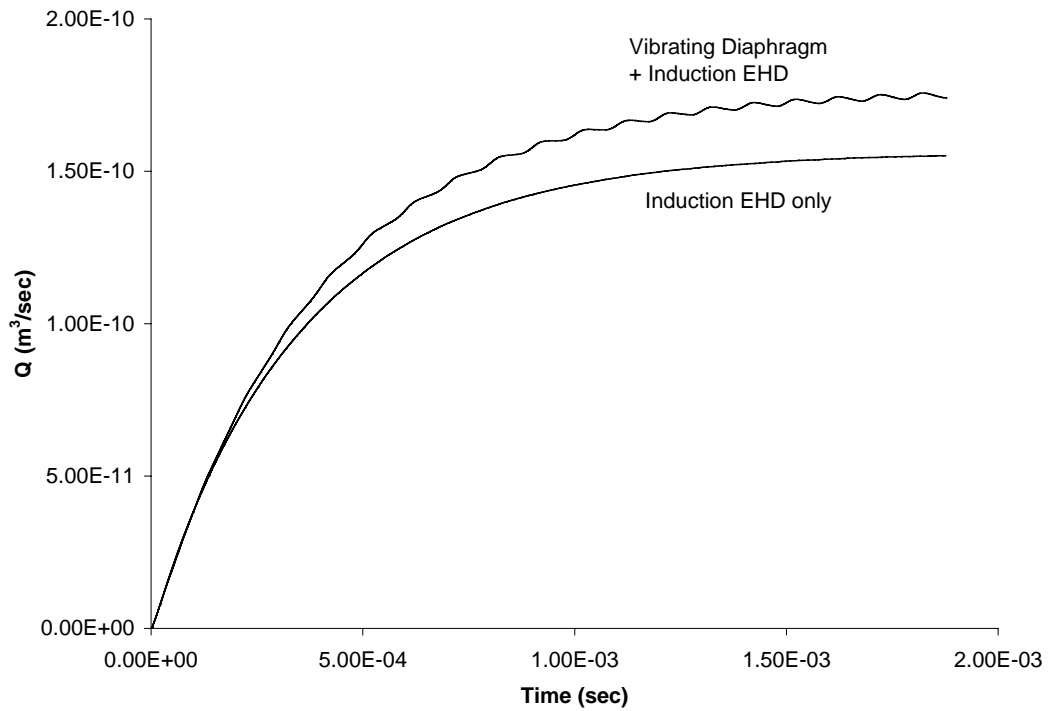
Figure 9: Flow due solely to induction EHD obtained from simulations using (a) three different mesh sizes, and (b) two different mesh sizes.

Figure 10: Comparison of flow due to combined action of vibrating diaphragm and induction EHD action to that from action solely of induction EHD for pumps of width (a) 100 μm, and (b) 200 µm.